On the effect of geometrical imperfections and defects on the fatigue strength of cellular lattice structures additively manufactured via Selective Laser Melting

M. Dallago, B. Winiarski, F. Zanini, S. Carmignato, M. Benedetti

Abstract

Porous structures have great potential in the biomedical field because, compared to traditional fully dense implants, prostheses with a porous structure show reduced stress shielding and improved osseo-integration. The development of Selective Laser Melting (SLM) made possible to obtain metallic cellular materials with highly complex structures characterized by a wide range of cell morphologies that allow to finely tune the mechanical properties of the implant to the patient needs. Nevertheless, there are still several issues to address: among others, detrimental residual stresses and the discrepancy between the as-designed and the manufactured geometry. Micro X-ray computed tomography (uCT), being an accurate non-destructive measuring technique, combined with the Finite Elements (FE) method permits to carry out in-depth investigations on the effect of the number and severity of defects on the mechanical properties. The current study is an investigation of the effect of the geometrical defects of a regular cubic lattice structure on the fatigue resistance at 10^6 cycles and on the elastic modulus. We compared the results of fatigue and quasi-static test with FE calculations based on the as-designed geometry and on the as-built geometry reconstructed from uCT scans. We observed that both the elastic modulus and the fatigue resistance are strongly correlated with the number and severity of defects and that predictions on the mechanical properties based on the as-designed geometry are not accurate. We thus highlight the importance of considering the limitations in accuracy of the manufacturing technique when designing load bearing lattice structures.

1. Introduction

The necessity for stiff, strong and light materials is mandatory in the aeronautics, automotive, sports and biomedical sectors and the class of foams and cellular materials can provide these properties. These materials are structures on the small scale, but they behave as homogeneous materials on the macroscopic scale. The main distinction is that the former have a random structure generally obtained by a process which allows limited control on the cell size and cell-wall thickness while the latter have a well determined periodic geometry which can be completely determined by a small number of parameters [Ashby, 2006; Fleck, 2010; Gibson, 1997]. In principle, a more controllable structure leads to more controllable mechanical properties and this makes cellular materials very versatile as their properties can be varied on a wide range by simply modifying the geometrical parameters on the small scale given the same base material [Gibson, 1997].

Porous structures have great potential in the biomedical field because, compared to traditional fully dense implants, prostheses with a porous structure show reduced stress shielding and improved osseo-integration [Dabrowski, 2010, Tan, 2017, Ahn, 2017]. The development of

Additive Manufacturing (AM) gave a great boost to the research and development of cellular structures for biomedical applications. In fact, with AM it became possible to obtain cellular materials also with highly complex structures characterized by a wide range of cell morphologies that allow to finely tune the mechanical properties [Murr, 2010; Murr, 2012; Rashed, 2016]: for example, costumer-specific implants and implants with a functionally graded structure (non-homogeneous distribution of the mechanical properties) that locally vary their properties to match those of the patient's bone can be easily manufactured [Khanoki, 2012; Khanoki, 2013]. Nowadays, metals are the best choice base materials for load bearing biomedical implants [Ryan, 2006, Singh, 2010, Wu, 2014] and the α+β Ti6Al4V alloy is one of the most popular because of a good combination of strength and ductility [Rack, 2006]. Among the various AM techniques for metals, Selective Laser Melting (SLM) allows greater precision [Tan, 2017] and was employed to produce the specimens object of this study.

Although SLM has been proven capable of producing structures of great complexity, there are still several issues to address. For instance, Ti6Al4V as-built SLM components are affected by detrimental residual stresses [Leuders, 2013] and a brittle martensitic α' microstructure [Vrancken, 2012; Qiu, 2013; Benedetti, 2017; Dallago, 2018]. Hot Isostatic Pressing (HIP) is a thermomechanical treatment that consists in simultaneously applying a high temperature and pressure by submerging the component in a fluid with the effect of relieving residual stresses, increasing the ductility of the microstructure (α' martensite is decomposed into α lamellae in a β matrix and the grains are coarsened) and reducing closed porosity [Leuders, 2013; Qiu 2013; Wauthle, 2015; Zhao, 2016a; Tammas-Williams, 2016; Van Hooreweder, 2017; Benedetti, 2017; Dallago, 2018]. Geometrical defects are also an issue because they are inevitably introduced into the printed structures and these can affect the mechanical and biological properties. Discrepancy between the as-designed and the manufactured geometry is a well-known phenomenon in biomedical metallic lattices characterized by strut thicknesses of a few hundred microns, which is close to the manufacturing limits [Parthasarathy, 2010; Van Bael, 2011; Liu, 2017; Bagheri, 2017]. Micro X-ray computed tomography, being an accurate non-destructive measuring technique [Wits, 2016; Khademzadeh, 2016], combined with the FE method permits to carry out in-depth investigations on the effect of the number and severity of defects on the mechanical properties. For instance, Liu et al. (2017) showed that FE models based on the as-built geometry of cellular lattices acquired via uCT scans can explain the mismatch between the mechanical properties measured experimentally and those predicted with simulations based on the as-designed geometry. The thickness of the as built strut of the cellular lattice, and so the deviation from the as-designed thickness, is determined by the size of the melt pool which is the result of the complex interaction of the local thermal properties of the powder/solid system and the SLM process parameters such as the laser power, the scanning speed [Mullen, 2009; Qiu, 2015; Sing, 2018] and layer thickness [Sing, 2018]. To complicate the matter, not only the as-designed size of the strut is relevant, but also its inclination is a factor to consider, as discussed in [Mullen, 2009; Emmelmann, 2011; Pyka, 2013; Yan, 2014; Kessler, 2017]. In fact, inclined struts are supported by loose powder which has lower thermal conductivity than the solid and thus a higher fraction of the powder is partially or completely melted compared to a vertical strut. The difficulty in predicting the as-built shape is further increased by the material shrinkage during solidification and cooling [Zhu, 2017].

Fatigue resistance is a critical aspect when load bearing biomedical implants are considered [Zhao 2016b]: consider, for example, the periodic nature of human gait in the case for hip implants [van den Bogert, 1999; Murr, 2010]. Nevertheless, few studies on the fatigue resistance of cellular

materials have been published until now compared to those on the static mechanical. Experimental studies on foams [Banhart, 1999; Gibson, 2000; Zettl, 2000; Zenkert, 2006] are more abundant than those on regular cellular materials, which mainly concern metallic AM lattices for biomedical applications [Hrabe, 2011; Leuders, 2013; Yavari, 2015, Zargarian, 2016]. These publications are mainly aimed at the determination of the S-N curves of structures with specific morphologies. The detrimental effect of geometrical irregularities as stress raisers on the fatigue resistance of AM metallic cellular structures has been observed in Hrabe (2011), Yavari (2013), de Krijger (2017). Ti-alloys in general have high notch sensitivity (Long, 1998; Niinomi, 2008), so fatigue resistance is strongly influenced by defects that act as stress raisers (Leuders, 2013; de Krijger, 2017). Fatigue is in fact caused by the accumulation of damage at spots where stress concentration occurs and thus to be able to accurately predict the fatigue resistance of a structure the focus must be shifted to the local details in geometry [Fricke, 2003; Dowling, 2013]. The stress concentration factor due to the joints and geometrical irregularities in general (roughness and variations in the cross-section of the cell-walls) was included in the approach based on numerical simulations described in Hedayati (2016) to estimate the fatigue life of cellular structures.
In this work, we investigated the fatigue strength and the elastic modulus of SLM Ti6Al4V regular cubic lattice specimens. Moreover, we studied the effect of the geometrical defects introduced into the lattice during the manufacturing process on the mechanical behavior. The morphology of the as-built lattice was acquired with a metrological micro X-ray computed tomography (uCT) and a statistical analysis was carried out on the point cloud obtained from the scanner to measure and classify the geometrical defects in terms of an as-designed/as-built mismatch. The detailed information on the specimen geometry was also used to devise FE models to compare the elastic modulus and the stress distribution at the junctions of the as-designed lattice and the as-built lattice. The residuals stresses were measured using the Plasma FIB-SEM-DIC micro-hole drilling method [Winiarski, 2016] in a region of interest located with a helical scanning trajectory µCT system.

2. Experimental

2.1 Cellular specimen

In this work, we studied regular cubic cellular lattices (Figure 2.1-1). The specimens were designed aiming at eliminating every sharp notch to improve fatigue resistance and obtaining an elastic modulus matching that of trabecular bone (~3 GPa) because the application we focused on is the production of fatigue resistant fully porous orthopaedic implants. The cell walls, of length L, are circular in cross-section (diameter t_0) and are joined with filleted junctions (radius R), as shown in Figure 2.1-1a. The values of the geometrical parameters are reported in Figure 2.1-1b. The nominal relative density of the lattice is 6.61%. The cellular part of the specimen is made to fill a cylindrical volume of 10 mm in diameter and 13.5 mm in height. The specimen is provided with threaded heads to allow both tensile and compressive loads (Figure 2.1-1c).

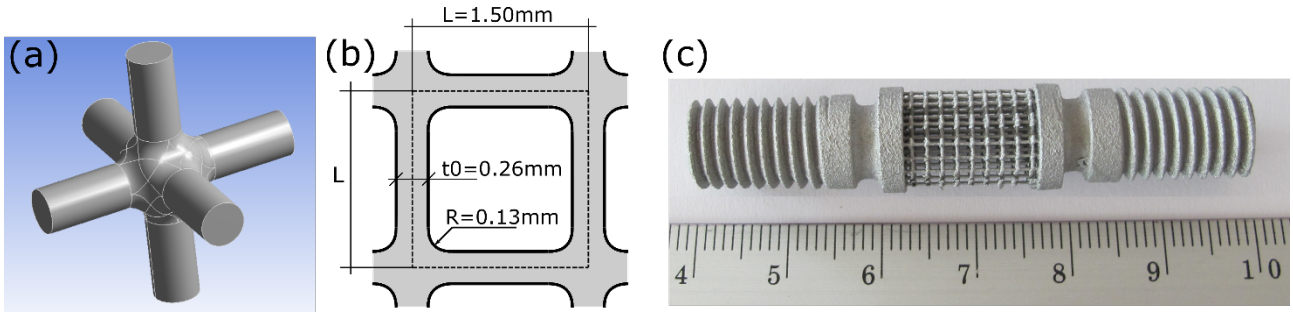

Figure 2.1-1. Cellular specimen studied in this work: (a) as-designed unit cell; (b) geometrical parameters of the unit cell; (c) entire specimen with threaded heads.

The specimens were additively manufactured via SLM with a 3D System ProX DMP 300 printer [Benedetti, 2017], starting from biomedical grade Ti6Al4V ELI (Grade 23) powder of mean diameter of 8.6 µm. The specimens were built inclined of 45° to the printing direction (Figure 2.1-2a), with one set of struts (identified with the *x* direction) laying in the printing plane and the other two sets inclined of 45° (Figure 2.1-2b). Two batches were prepared: the first was stress relieved at 670°C for 5 h in Ar protective atmosphere (referred to as "stress relieved" in the text), while the second one was treated by hot isostatic pressing (HIP) at 920 °C and 1000 bar for 2 hours after sand blasting to remove the loose particles (referred to as "HIPed" in the test). Further details on the design procedure of the specimens' geometry and on the manufacturing process are provided in [Dallago, 2018] and [Benedetti, 2017].

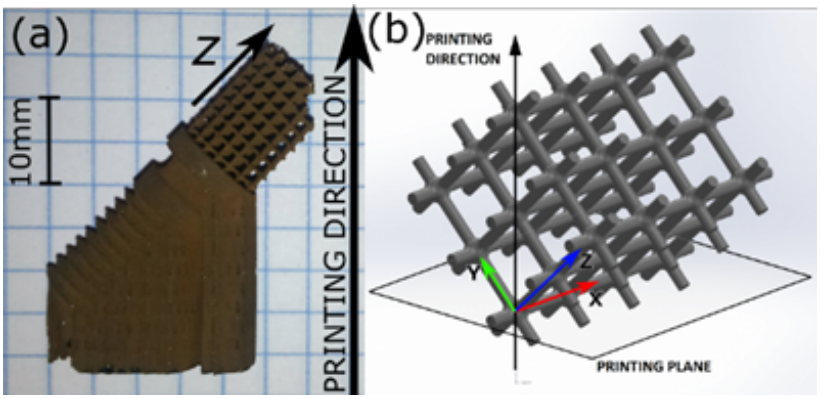

Figure 2.1-2. (a) As-built specimen with support structure; (b) details on the orientation of the struts to the printing direction and *xyz* reference system.

2.2 Metrological analysis

A HIPed specimen was scanned using a metrological CT system (Nikon Metrology MCT225) characterized by micro-focus X-ray tube, 16-bit detector with 2000×2000 pixels, high-precision linear guideways and controlled cabinet temperature (20±0.2 °C). The three-dimensional model of the specimen was reconstructed with a voxel size of 8.3 µm. The high-density point cloud generated by the scanner was fed to an in-house Matlab (MathWorks, USA) routine to measure the geometrical features of the as-built lattice (a flowchart describing the basic characteristics of the routine is showed in Figure 2.2-1). As a first step, the centers of the junctions between the struts were estimated as the centroid of the data points of the 6 struts converging in the junction. This is

the most important step because all the others depend on it. The position of the center of the as-designed lattice was used as a first guess to find the six struts converging into the selected junction. The position of the centers was used to carry out a general comparison of the as-built geometry with the as-designed geometry by overlaying the two by minimizing the sum of the squares of the distances between corresponding junction centers. This operation made possible to capture also qualitatively the as-built/as-designed mismatch strut by strut, junction by junction. Slices were sampled along the axis of each strut and the points were fitted with both circles and ellipses. The parameters registered in such way were analyzed statistically to characterize the as-built geometry and passed on to a FE code made of beam elements to study the effect of the as-built geometry on the mechanical behavior of the lattice.

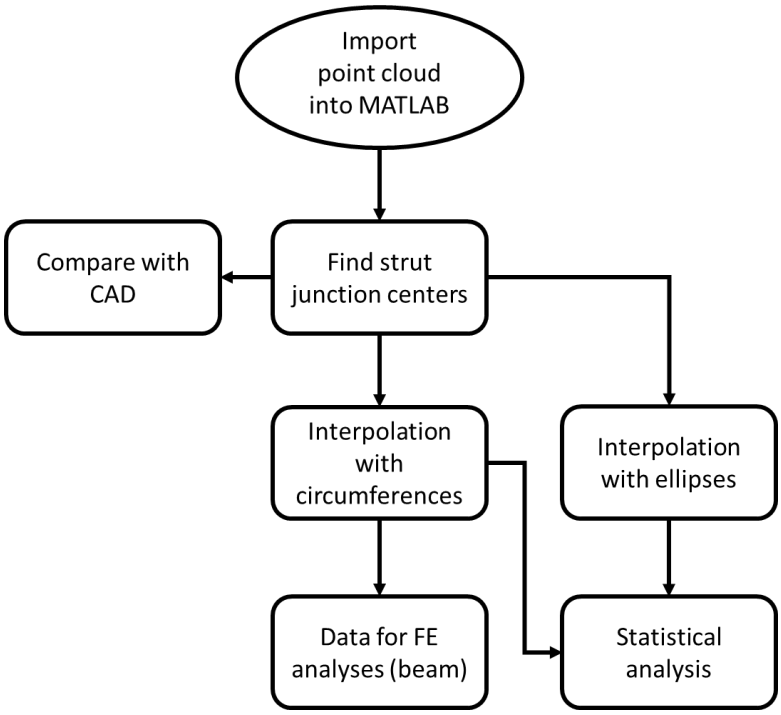

Figure 2.2-1. Flowchart of the Matlab routine used to analyze the point cloud generated by the uCT scanner.

2.3 Residual stresses

Residual stresses in a stress relieved specimen were measured using the Plasma FIB-SEM-DIC micro-hole drilling method. After micro X-Ray CT helical scanning (FEI Heliscan µCT scanner) and reconstruction of the whole scaffold, we have selected a suitable region of interest near a junction (A, in Figure 2.3-1) to measure the residual stresses in the circumferential and axial directions of the strut. Later, we removed material near the junction (Figure 2.3-1b and 2.3-1c) to create the flat and smooth surface needed for reliable measurements with the micro-hole drilling method. We have used PFIB at 30kV/1.3µA for about 3 hours of continuous milling. Next, an array of submicron-holes (diameter ~400-800 nm) were milled with a PFIB using a bitmap file with predefined random pattern. The submicron-holes obtained after such procedure work in a similar way as Pt nano-dots, thus enhancing the topological contrast of FEGSEM imaging and improving the accuracy of DIC displacement/strain measurement [Winiarski, Schajer et al., 2012]. Finally, two micro-holes 20 µm in diameter and 10 µm deep (1 and 2 in Figure 2.3-1d) were milled (15 nA at 30 kV). The dimensions of the holes were selected so that the surface topography (roughness) after site

preparation is much smaller than the micro-hole dimensions. In the stress mapping process, a sequence of three FEGSEM images (dwell time, Dt = 3µs, 8 frames averaged, ETD detector) of the patterned areas were acquired at 0° stage tilt before milling and three images after milling.

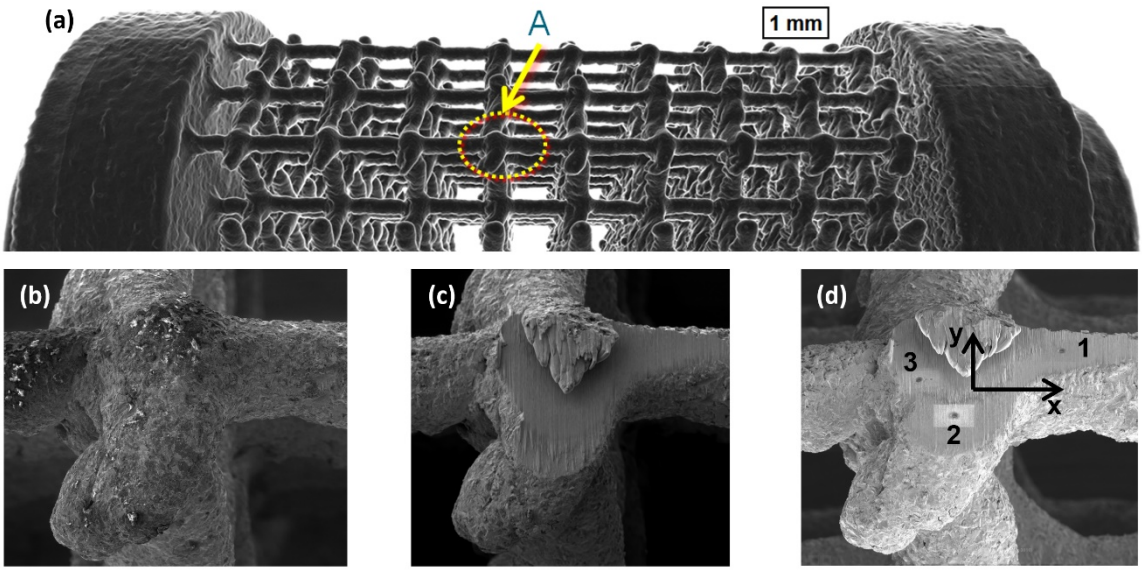

Figure 2.3-1. Shows position of residual stress measurements with the micro-hole drilling method; (a) shows volume rendered of reconstructed micro CT projections, where A indicates the measurements location, (b) and (c) shows the junction before and after preparation for the measurements, (d) shows locations of micro-holes 1 and 2, while micro-hole 3 is used for testing milling conditions before actual measurements.

The radial displacement $\delta(r,\theta)$ of the surface around a circular hole of diameter a drilled in a uniformly stressed material with dimensions much greater than the hole size have a trigonometric form [Schajer, Winiarski et al., 2013] (E is the Young's modulus):

$$\frac{\delta_r(r,\theta)}{a} = \frac{\left[P \cdot u_r(r) + Q \cdot v_r(r) \cdot \cos(2\theta) + T \cdot v_r(r) \cdot \sin(2\theta)\right]}{E} \tag{2.3-1}$$

where the stresses

$$P = \frac{(\sigma_x + \sigma_y)}{2} \qquad Q = \frac{(\sigma_x - \sigma_y)}{2} \qquad T = \tau_{xy} \tag{2.3-2}$$

respectively represent the isotropic stress, the 45° shear stress, and the axial shear stress. In Eq. (2.3-1), $u_r(r,\theta)$ is the radial profile of the radial displacements caused by a unit isotropic stress P, and $v_r(r,\theta)$ is the radial profile of the radial displacements caused by unit shear stresses Q or T.

The corresponding circumferential displacements have the following form:

$$\frac{\delta_\theta(r,\theta)}{a} = \frac{\left[P \cdot u\theta(r) + Q \cdot v_\theta(r) \cdot \cos(2\theta) + T \cdot v_\theta(r) \cdot \sin(2\theta)\right]}{E} \tag{2.3-3}$$

where $v_\theta(r,\theta)$ is the radial profile of the circumferential displacements caused by unit shear stresses Q or T.

The advantage of normalizing by the hole radius a and Young's modulus E (here 71.7 GPa) is that the radial displacement profiles $u_r(r)$ and $v_r(r)$ become non-dimensional. The resulting numerical values depend on hole depth and can be computed using finite element analysis [Winiarski, Withers et al., 2012].

After some mathematical rearrangements and correcting for SEM image stretch and shear artefacts, Eq. (1) can be expressed in a compact 9 × 9 matrix form (see the derivation of formula in [Schajer, Winiarski et al., 2013])

$$\overline{\boldsymbol{G}}^{\boldsymbol{T}}\,\overline{\boldsymbol{G}}\,\overline{\boldsymbol{w}} = \overline{\boldsymbol{G}}^{\boldsymbol{T}}\,\overline{\boldsymbol{\delta}} \qquad (2.3\text{-}4)$$

Where $\overline{\boldsymbol{G}}$ is a matrix of the radial profile of the radial displacements caused by a unit stresses P, Q and T; $\overline{\boldsymbol{G}}$ has $2N$ rows and 9 columns, where N is the number of pixels of the image used for DIC calculations; $\overline{\boldsymbol{w}}$ includes the correction for SEM image stretch and shear artefacts; $\overline{\boldsymbol{G}}^{\boldsymbol{T}}\overline{\boldsymbol{\delta}}$ (1 × 9 vector) are the products of the matrix coefficients and displacements at each pixel used for DIC calculations. Three images collected before the micro-hole milling and three after are used to average the measured stress components (σ_x, σ_y, τ_{xy}) from 9[1] data points. The uncertainty of the measurements of the three stress components is equal to the standard deviation of the 9 measured data points for each micro-hole.

2.4 FE modelling

The FE method (ANSYS 17.2®) was used to predict the mechanical behavior of the as-designed geometry of the lattice and to interpret the results of the mechanical tests in terms of the as-built geometry acquired from the metrological CT scans. We devised both models made of beam elements (3 node Timoshenko beam, BEAM189) and of solid elements (3D 10-Node Tetrahedral Structural Solid, SOLID187) to obtain different degrees of simplification. Only small-displacement linear elastic analyses were implemented to calculate the elastic modulus and the stress concentration factor K_t^* at the junctions (only with the solid model). The stress concentration factor was calculated according to the following definition (Eq. 2.4-1):

$$K_t^* = \frac{\text{maximum von Mises equivalent stress in the structure}}{\text{nominal homogeneous stress}} \qquad (2.4\text{-}1)$$

Where the nominal homogeneous stress is the ratio between the load on the unit cell and the nominal area of the unit cell ($L \times L$). This quantity is useful because it relates the homogenized stress in the lattice with the maximum stresses acting in the base material.

2.5 Mechanical testing

Three specimens for both heat treatments were subjected to axial fatigue tests using a RUMUL Mikrotron 20 kN resonant testing machine equipped with a 1 kN load cell operating at a nominal

[1] Cross – correlation of 3 SEM image collected before (I_{b1}, I_{b2}, I_{b3}) and 3 after (I_{a1}, I_{a2}, I_{a3}) micro-hole drilling allows calculate 9 ($I_{b1} – I_{a1}$, $I_{b1} – I_{a2}$, $I_{b1} – I_{a3}$, $I_{b2} – I_{a1}$, $I_{b2} – I_{a2}$, etc.) displacement field maps later used for the residual stress calculation.

frequency of 120 Hz under load control. Constant amplitude fully reversed fatigue cycles (zero mean stress, $R = -1$) were applied to measure the fatigue strength at 10^6 cycles. This has been estimated according to a step loading procedure developed by Maxwell (1999) for Ti alloys that considerably reduces the testing time and the amount of expensive experimental material with respect to standard methods.

The fatigue notch factor K_f^* was calculated from the experimental measurements with Eq. 2.5-1:

$$K_f^* = \frac{\text{fatigue resistance of bulk specimen}}{\text{fatigue resistance of the cellular specimen}} \tag{2.5-1}$$

Where the fatigue resistance of each cellular specimen was calculated by dividing the load at failure by the nominal cross section of the specimen (i.e. the section measured as if the cellular material was a bulk material). This definition of the fatigue notch factor is based on the observation that the cellular specimen can be considered a notched specimen.

The elastic modulus was measured on two stress-relieved specimens as the slope of loading-unloading curves, according to ISO 13314. The specimens were mounted on an Instron 4500 testing machine with a 10 kN load cell and the displacement was measured with an axial extensometer. The speed of the cross-head was 0.5 mm/min.

A thorough description of the mechanical tests can be found in [Dallago, 2018] and, for brevity, we only provided the reader with some essential pieces of information.

3. Results and discussion

3.1 Metrological analysis

The point cloud generated by the uCT scanner (a detail is shown in Figure 3.1-1a, compared with the as-designed geometry) was used to carry out a thorough metrological analysis of the cellular lattice with an in-house Matlab routine. An *xyz* reference system with the axes parallel to the struts is defined to identify the three set of struts (Figure 3.1-1b); the *z* axis is aligned with the loading direction of the specimen (Figure 2.1-2a). The distance between the positions of the centers of the junctions of the as-built lattice (Figure 3.1-1c) and the corresponding centers of the as-designed lattice are measured to estimate the overall distortion of the lattice (Table 3.1-1). The average distance is low (35.5 um) if we consider that the unit cell size is 1500 um, and the maximum value confirms that the overall distortion of the lattice is not particularly severe. The junction centers were used to overlay the as-built lattice on the as-designed lattice (details of the outcome are shown in Figure 3.1-1a in 3D and in Figure 3.1-2 the *xy* plane in 2D) and this allows us to make some preliminary observations. The surface of the struts is highly irregular and specifically the struts laying in the printing plane (*x*-struts) show numerous protrusions.

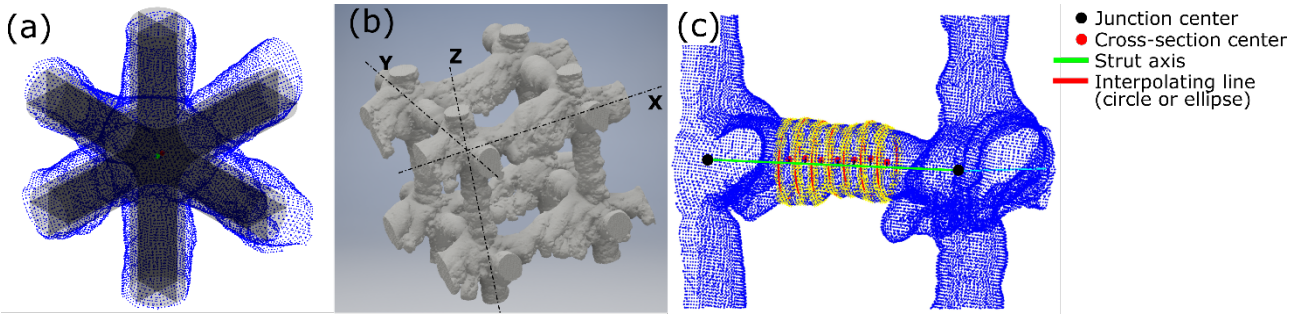

Figure 3.1-1. Details of the results of the uCT scan of the as-built lattice. (a) Overlay of an as-built unit cell (blue points) on the as-designed unit cell using the junction centers; (b) detail of the uCT scan with the *xyz* reference system; (c) CT data cloud with sections, section centers and strut axis highlighted. Note the waviness of the strut (offset between the section centers and the strut axis).

Table 3.1-1. Statistical descriptors of the misalignment of the junction centers.

Statistical parameter	Value [µm]
Maximum deviation	95.0
Minimum deviation	2.8
Mean	35.5
Standard deviation	18.4
Median	32.2

Ten sections were sampled along each strut of the specimen and the following geometric parameters were measured (for clarity, only seven shown in Figure 3.1-1c):

- Cross-section equivalent radius (calculated as the radius of the circumference with the same area as the strut cross-section).
- Cross-section eccentricity $e = \sqrt{a^2 - b^2} / a$, where a and b are the major and minor axis of the best fitting ellipse, respectively. $e = 0$ is a perfect circle, while $e = 1$ is a segment.
- Cross section orientation with respect to the *xyz* reference system.
- Offset of the cross-section center to the strut axis.

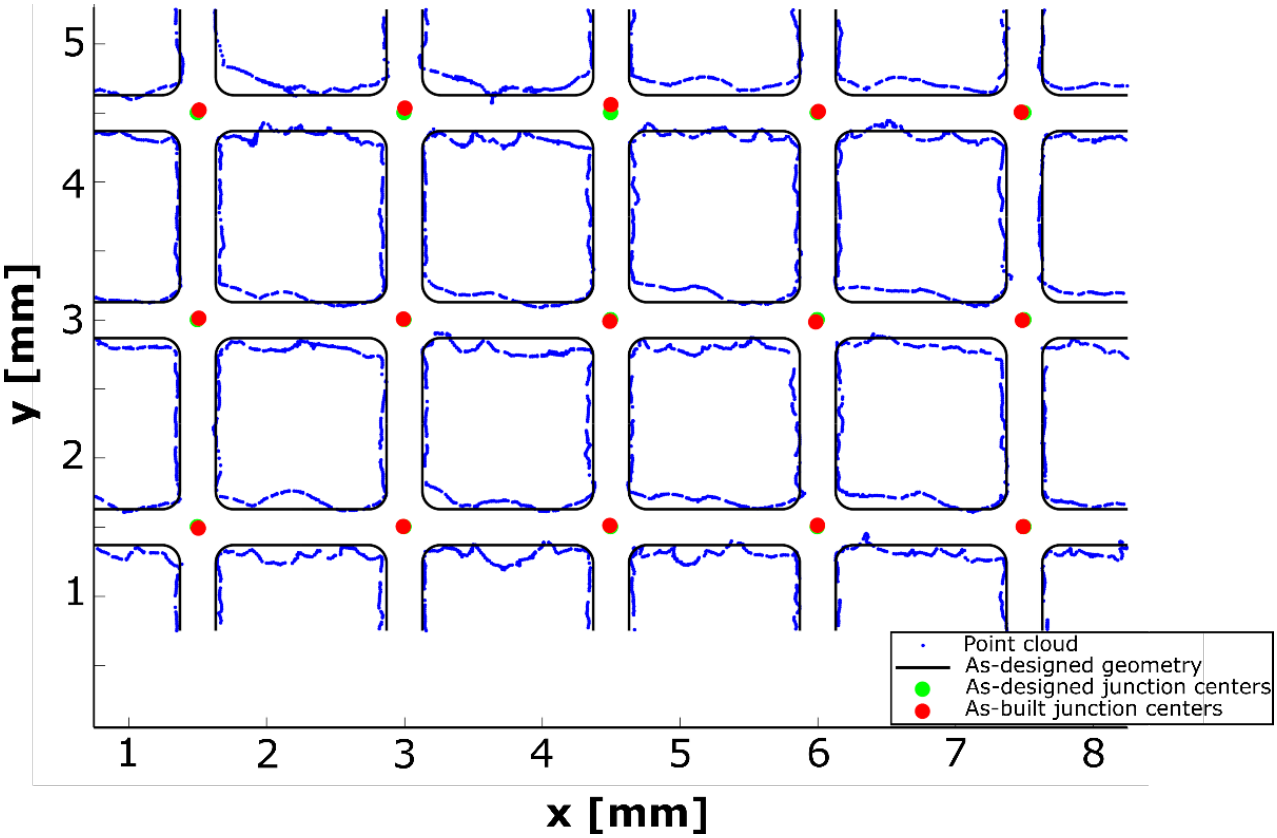

Figure 3.1-2. 2D view of the overlay of the as-built lattice (blue points) on the as-designed lattice (black lines) using the junction centers. Note the greater mismatch of the horizontal struts (*x*-strut, parallel to the printing plane) compared to the vertical struts (*y*-struts, printed at 45° to the printing plane).

A first appreciation of the as-designed/as-built mismatch is already possible from a visual comparison (Figures 3.1-1a and 3.1-2). The statistical analysis carried out on the quantities previously listed gave a quantitative measure of the uneven distribution of material in the as-built lattice, which is ultimately determined by the local heat transfer properties of the powder-solid material system and it manifests as a series of defects that affect the lattice. According to this analysis, the following defects could be identified and classified:

- Variable strut cross-section equivalent radius.
  The equivalent radius has the statistical distribution shown in Figure 3.1-3a, characterized by the descriptors listed in Table 3.1-2. The most notable aspect is that the average cross-section equivalent radius is always higher than the as-designed value. The struts parallel to the printing plane (*x*-struts) show the greatest mean deviation from the design value (51.8%) and the widest distribution. The wider the distribution, the less predictable is the outcome of the printing process.
- Offset of the cross-section centers from the axis connecting two (as-built) junction centers.
  This offset is manifested as waviness in the struts and again the struts parallel to the printing plane (*x*-struts) show the highest average offset (55.8%, Table 3.1-3) and the widest distribution (Figure 3.1-3b). In fact, the struts laying in the printing plane are highly irregular with numerous protrusions (which are possible to appreciate also visually, see Figure 3.1-2 for example) that offset the barycenter of the section.

- Strut cross-section eccentricity.
  The cross-section of the as-built struts deviates somewhat from the circular shape and tends to become elliptical. The eccentricity measures the deviation from the circular shape. The best fitting ellipses of the cross-sections are shown in Figure 3.1-4 for each strut set. A statistical analysis of the eccentricity was also carried out and we observed that most of the struts deviate from a circular section (Figure 3.1-3c). The struts laying in the printing direction (x-struts) are the most elliptical ($e = 0.79$, Figure 3.1-4a) and show an inclination of 45° to the y and z directions, exactly aligned with the printing direction. The statistical distribution of the inclinations (Figure 3.1-3d) is very narrow around angles of -45°, +45° and 135°. The y- and z-struts show a more uniform distribution of inclinations, although there appears to be a prevalent orientation (16° and 20°, respectively, Figure 3.1-3d). The small inclination of the cross-sections of the other struts indicates that most likely the specimen was not printed perfectly at 45° as indicated in Figure 2.1-2b.
- Missing/interrupted struts.
  We observed a few struts with considerable thinning in the cross-section, as shown in Figure 3.1-5. An excessive thinning may lead to the interruption of the strut: in this specimen, of 910 struts, two vertical struts are interrupted due to an excessive thinning of the section.
- Junction center position.
  Observing Figures 3.1-1 and 3.1-2, the uneven distribution of material in the proximity of the junction is immediately noticeable. Because of this, the junction centroids of the as-built lattice don not coincide with those of the as-designed lattice and there is a 35±18 µm offset on average, which is quite small compared to a 1500 µm unit cell size. Some statistical parameters of the as-built/as-designed junction center offset are reported in Table 3.1-1.

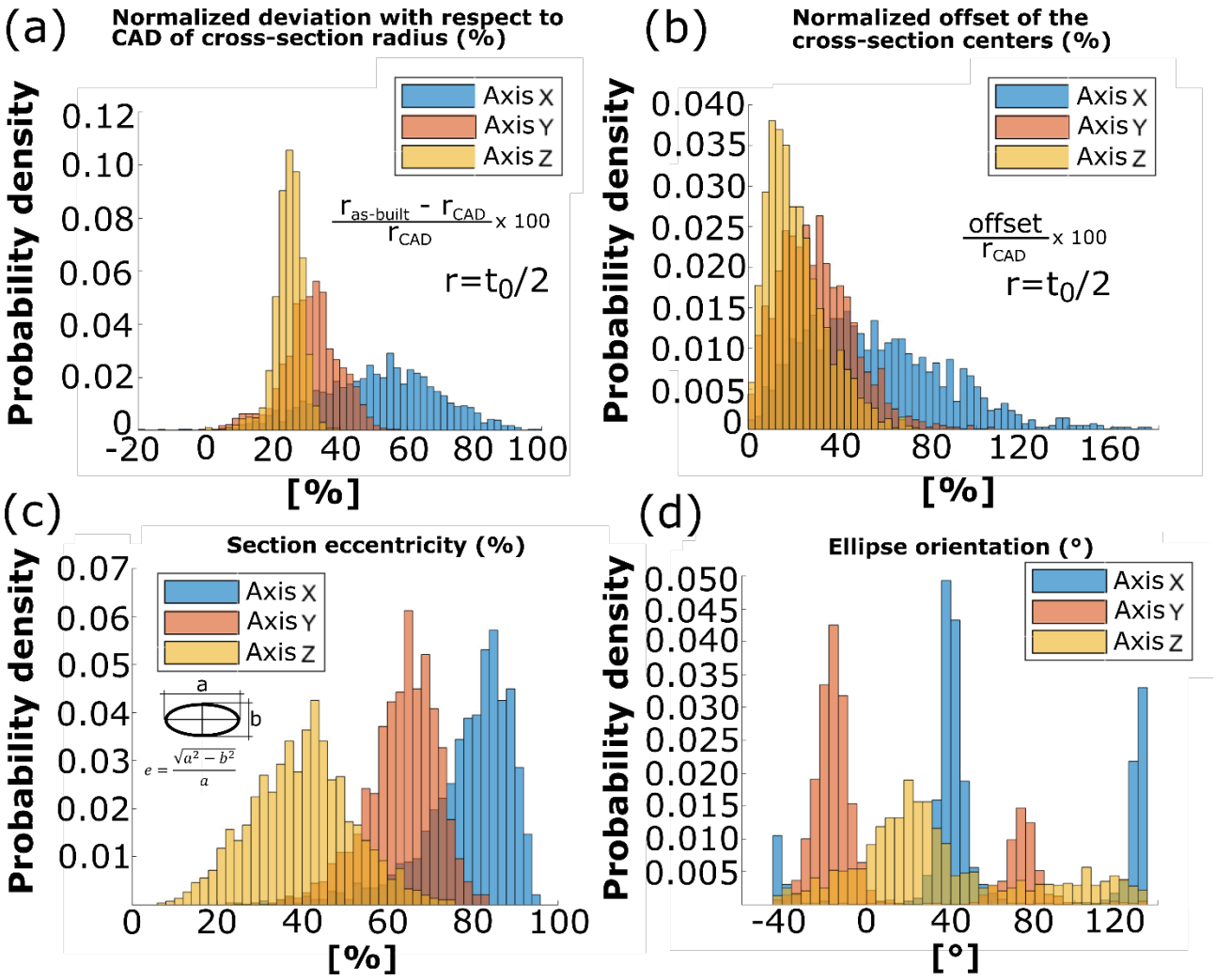

Figure 3.1-3. Results of the statistical analysis carried out on the uCT point cloud: (a) distribution of the normalized deviation between the as-built equivalent cross-section radius and the as-designed value (0.130 mm) in % ; (b) distribution of the normalized offset of the centers of the fitted circumferences from the strut axis; (c) distribution of the eccentricity values calculated form the ellipses fitted on the sampled cross-sections; (d) distribution of the orientations of the best fitting ellipses.

Table 3.1-2. Statistical descriptors of the cross-section radius variation (CAD: $t_0/2 = 0.130\mu m$).

Statistical parameter	Cross-section radius variation					
	X [µm]	Y [µm]	Z [µm]	X [%]	Y [%]	Z [%]
Max. value	128.1	73.2	50.9	98.6	56.3	39.2
Min. value	-23.9	-0.18	-16.2	-18.4	-0.13	-12.5
Mean	67.3	40.8	32.2	51.8	31.4	24.8
Std. Dev.	22.3	11.0	5.90	17.20	8.50	4.50
Median	68.3	41.3	32.6	52.5	31.8	25.0

Table 3.1-3. Statistical descriptors of the cross-section center offset.

Statistical parameter	Cross-section center offset					
	X [µm]	Y [µm]	Z [µm]	X [%]	Y [%]	Z [%]
Max. value	226.2	139.4	96.1	174	107.3	73.9
Min. value	1.5	1.3	0.2	1.2	1.0	0.2
Mean	72.6	38.5	27.7	55.8	29.6	21.3

Std. Dev.	39.9	21.1	16.9	30.7	16.2	13.0
Median	67.3	36.5	23.8	51.8	28.1	18.3

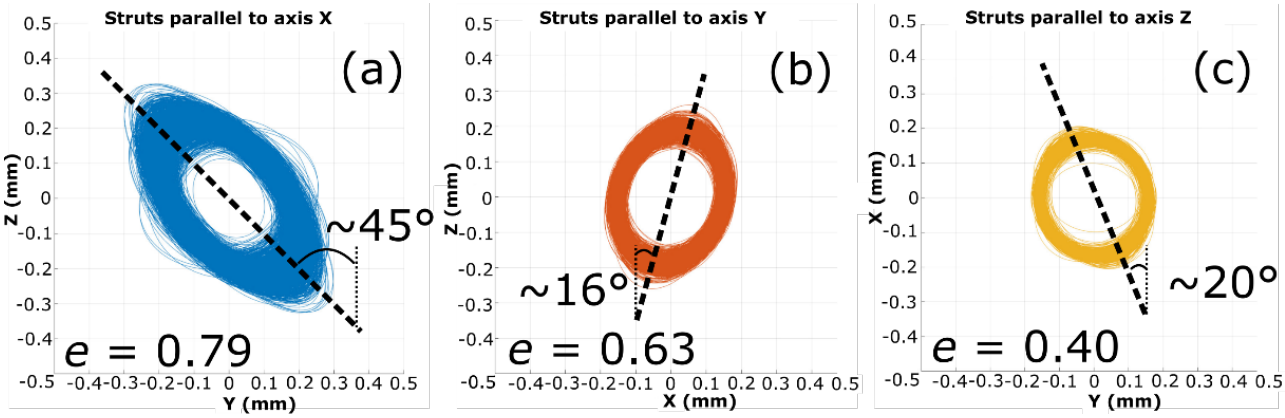

Figure 3.1-4. Plot of the best-fitting ellipses of the cross-section of each set of struts. The centers of the sections of each strut are translated to the (0,0) point with the correct inclination to the other two set of struts indicated by the *xyz* reference system. (a) x-struts; (b) y-struts; (c) z-struts.

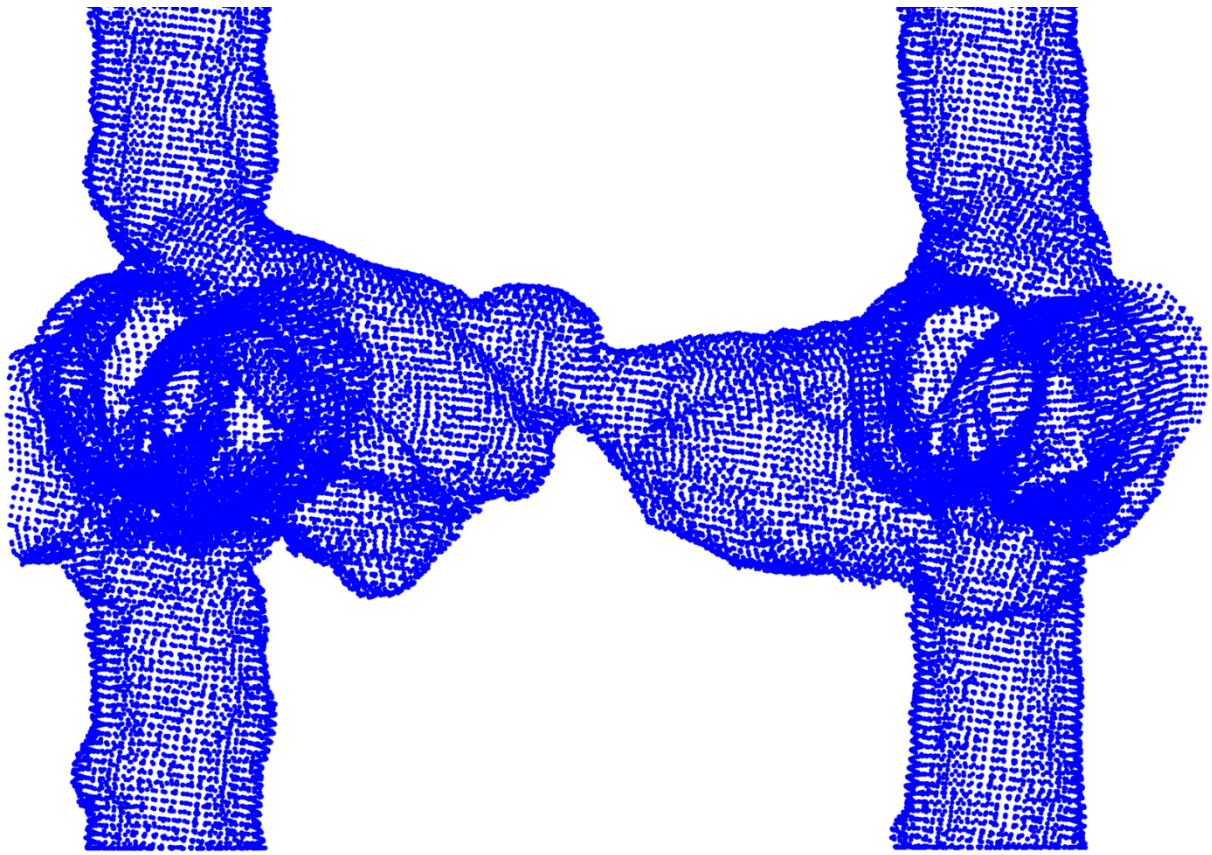

Figure 3.1-5. Example of a strut (*x*-strut) with considerable thinning in the cross-section.

3.2 Residual stresses

The residuals stresses in a stress relieved specimen were measured using the Plasma FIB-SEM-DIC micro-hole drilling method. Detrimental tensile residual stresses were found in the surface regions

of the junction in location 1 in the circumferential direction ($\sigma_y = +200 \pm 80 MPa$) and in the axial direction ($\sigma_x = +100 \pm 70 MPa$). While in location 2, both tensile and compressive residual stresses were present: $\sigma_x = +300 \pm 100 MPa$ and $\sigma_y = -100 \pm 70 MPa$ (see coordinates in Fig. 2.3-1d).

3.3 Elastic modulus

The elastic modulus of bulk Ti6Al4V specimens was measured in Benedetti et al., 2017 and the results are reported in Table 3.3-1 for both heat treatments. Quasi-static testing was carried out only on stress relieved cellular specimens, thus FE analyses were performed only with the elastic properties of the stress relieved Ti6Al4V ($E = 113\ GPa$, $\nu = 0.34$).

Table 3.3-1. Elastic moduli of the bulk material for both heat treatments. The elastic moduli were measured in specimens printed along their longitudinal direction [Benedetti et al., 2017].

	Stress relieved	HIPed
E	113 MPa	110 MPa

A solid FE model of the as-designed unit cell was used to estimate the expected elastic modulus of the structure, by applying periodic boundary conditions as described in [Kim, 2003] implemented as in Figure 3.3-1a by constraining the displacements of master nodes defined on the sections of the struts. Solid models of the as-built structure were also devised by meshing the eight junctions extracted from the uCT scan. We chose these set of BCs (Figure 3.3-1b) because, in our opinion, PBCs are not appropriate in this case because the structure is not strictly periodic anymore (given the irregularities). On the other hand, it is reasonable to assume that the horizontal struts are unloaded while the vertical struts are constrained to deform along the vertical axis by the other vertical struts. Note that applying these set of BCs to the as-designed unit cell would give the same elastic modulus as with the PBCs given the perfect symmetry of the as-designed geometry.

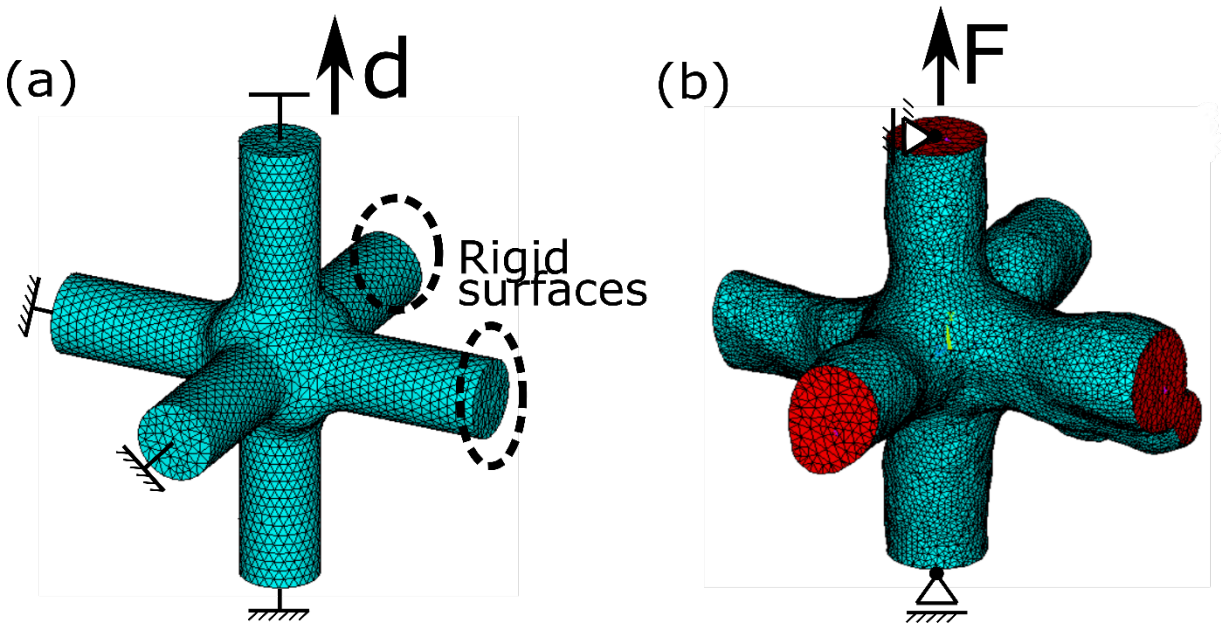

Figure 3.3-1. Solid FE models and boundary conditions to calculate the elastic modulus: (a) as-designed unit cell; (b) example of as-built unit cell.

Solid models are the most accurate, but they are very computationally demanding. To overcome this limitation, we used the results of the μCT scan to build models made of beam elements of the entire specimen that include the geometrical defects of the as-built lattice. Four such models were created, of increasing complexity, to compare the effect of the different types of defects (in the first three models, the centers of the junctions are in the as-designed location):

- Beam model with variable cross-section diameter and zero center offset.
- Beam model with variable cross-section center offset and constant diameter, equal to the mean value calculated form the CT data (the mean values are different for struts of different orientation).
- Beam model that combines the two previous defects.
- Beam model that includes all the defects: variable cross-section diameter and offset, missing struts and the junction centers location as calculated form the μCT data.

Although not useful to estimate the stresses, these models allowed us to get some more insight into the effect of defects on the elastic modulus of the lattice. Each strut was meshed with beam elements with a circular cross-section and the section properties (diameter and center offset from the mean axis) assigned based on the statistics extracted from the μCT data (the beam model and its details are shown in Figure 3.3-2). The strut thickness (diameter) and the offset were assigned randomly from a normal distribution defined by the mean value and the standard deviation calculated from the μCT data analysis (Figures 3.1-3a and 3.1-3b). The offset is defined by a vector of modulus extracted from the distribution of Figure 3.1-3b and direction an angle θ chosen randomly between 0° and 360° (Figure 3.3-2). It should be noted that the distributions of the offset in Figure 3.1-3b are not strictly normal, but for simplicity we assumed that they are. We simulated the compression tests by applying a small uniform displacement to the top side of the model and by fixing the bottom side, as shown in Figure 3.3-2. The simulations were repeated 15 times for each model type to achieve a suitable statistic.

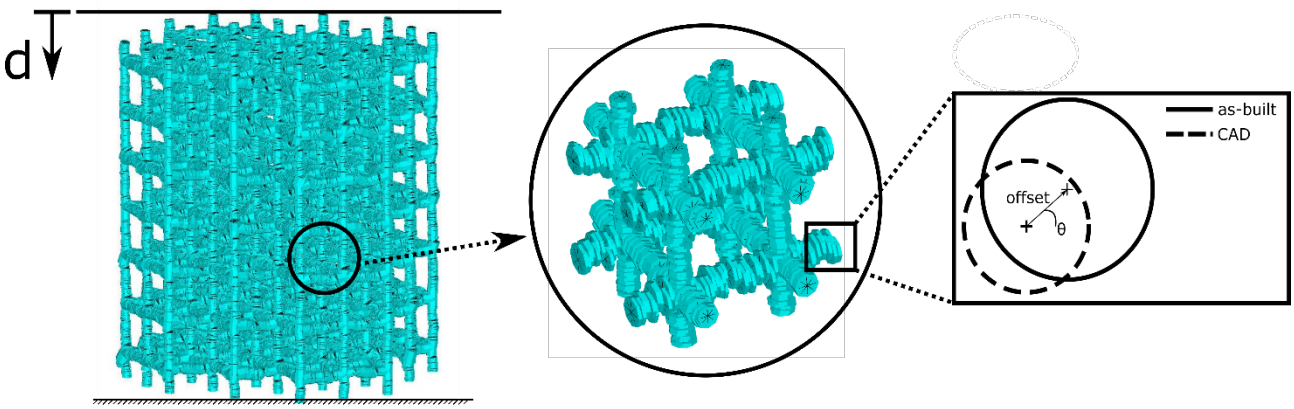

Figure 3.3-2. Beam model of the cellular part of the specimen, including geometrical defects. The struts are meshed with beam elements of circular cross-section and a random offset from the axis joining two junctions.

The comparison of the results of the various simulations give us some appreciation of the role of the geometrical defects on the elastic modulus (Figure 3.3-3). The as-designed model (3111 MPa) with

PBC considerably underestimates the elastic modulus of the as-built structure (3436 MPa). This mismatch is due to the combined effect of the defects in the as-built structure, predominantly due to the thicker struts of the as-built lattice. On the other hand, the elastic modulus of an ideal unit cell with the struts thickness equal to the as-built mean values is well over 4000 MPa, regardless of the fillet radius (Dallago, 2018). In fact, the analysis of the results of the beam models can resolve the contribution of the different types of defects:

- the offset of the cross-section centers (strut waviness) causes a remarkable drop in the elastic modulus (3870 MPa) compared to the model that accounts only for the cross-section diameter statistical distribution (4379 MPa);
- the cross-section diameter statistical distribution does not seem to have a significative effect on the elastic modulus;
- the misalignment of the junction centers further decreases the elastic modulus to 3659 MPa;
- Including also the missing struts, the elastic modulus becomes 3491 MPa, which is very close to the experimental value.

In conclusion, the increase in the mean cross section diameter has the obvious effect of increasing the elastic modulus, but it also appears that the width of the cross-section diameter distribution does not have a significant effect (very small standard deviation in the results of the beam models). The strut waviness and the misalignment of the junction centers significantly decrease the elastic modulus while the missing struts, even if parallel to the loading direction, do not have a major effect, if they are few compared to the total number of struts (two, in our specimen). This is because the strut waviness and the misalignment of the junction centers introduce bending loads in the lattice. It is likely that a stretching dominated lattice such as the one considered in this work, is particularly sensitive to these types of defects. The results of the solid FEM model based on the CT scans are reasonably close to the experimental value, although slightly higher. This is most likely because only unit-cell sized models could be simulated, that cannot correctly reproduce the complex interaction between the various defect types.

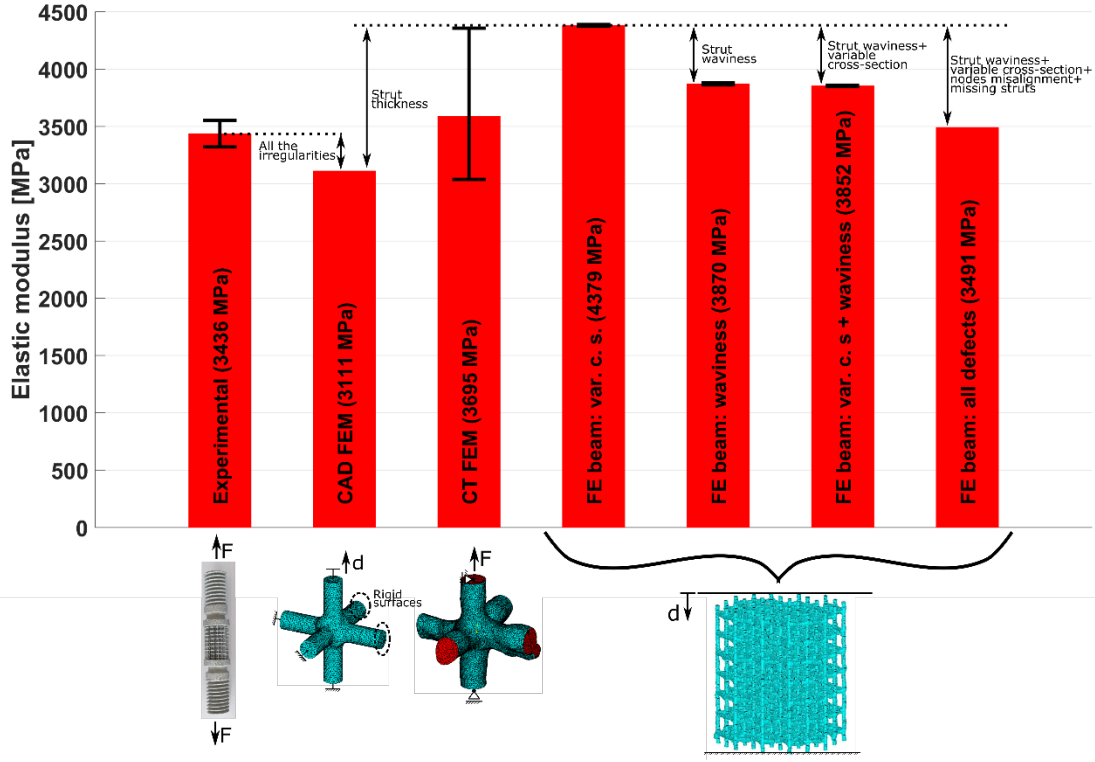

Figure 3.3-3. Bar chart comparing the elastic moduli calculated by the various FE models with the experimental measurement.

3.4 Fatigue strength

The fully reversed fatigue strength at 10^6 cycles of unnotched bulk SLM specimens, printed with the same process parameters as their cellular counterpart, have been studied and are discussed in [Benedetti, 2017], but the results relevant to this work are reported in Table 3.4-1 for simplicity.

Table 3.4-1. Fully reversed fatigue strength at 10^6 cycles properties of bulk Ti6Al4V [Benedetti, 2017].

	Stress relieved	HIPed
$\sigma_{a,10^6}$	240 MPa	380 MPa

The mechanical properties of the base material and the as-designed geometrical parameters are used to calculate the expected mechanical properties of the as-built lattice. The stress concentration factor K_t^* of the as-designed unit cell was calculated with a linear elastic FE analysis to be 65 (the boundary conditions applied are those of Figure 3.3-1a). Assuming a conservative notch sensitivity q for SLM titanium equal to 1, the expected fatigue notch factor K^*_f is equal to the stress concentration factor [Dowling, 2013]:

$$K_f^* = 1 + q\left(K_t^* - 1\right) = 65$$

The fatigue strength of the cellular specimen is calculated from Eq. 1 for both the HIPed and the stress relieved structures.

$$\sigma_a^{cell} = \frac{\sigma_a^{bulk}}{K_f^*}$$

The fatigue strength and the fatigue notch factor calculated based on the as-designed geometry are reported in Table 3.4-2.

Table 3.4-2. Fatigue properties calculated based on the as-designed geometry.

	Stress relieved	HIPed
$\sigma_{a,10^6}$	3.4 MPa	5.4 MPa
K^*_f	65	65

The results of the fatigue tests are provided in Table 3.4-3 together with their standard deviation. The fatigue notch factor is calculated from the experimental data according to Eq. 2.5-1. The effect of HIPing is not significative on the fatigue resistance because both values are within the bounds of the standard deviation. Arguably, the clear improvement induced by HIPing on the fatigue strength of the bulk specimens is not matched in the cellular lattices because although it is effective in closing the internal porosity in the struts [Dallago, 2018], it does not reduce the severity of the surface irregularities. That is, we observe that the fatigue resistance of the cellular structures is controlled by the surface quality in terms of roughness and especially notches and not by the size of the internal pores. Moreover, the experimental fatigue notch factors are two to three times higher than the expected values and, in our opinion, this indicates that the notches introduced in these structures by the manufacturing process considerably increase the severity of the strut junctions compared to the as-designed geometry. The junctions between the struts are indeed the most critical part for fatigue in this kind of structures, given that the struts always break at the junctions [Dallago, 2018].

Table 3.4-3. Fatigue properties measured experimentally.

	Stress relieved	HIPed
$\sigma_{a,10^6}$	2.06±0.21 MPa	2.02±0.37 MPa
K_f^*	116	188

An estimation of the stresses acting at the strut junction in the as-built lattice could be carried out by selecting eight junctions (of the size of a unit cell) from the CT scan of the entire specimen and importing them into Ansys. Due to limitations in computational power, the FE analysis was limited to a single junction. These models were solved by applying the displacements on the extremities of the struts (on the "cuts"), obtained from the solution of the beam model that most accurately represents the specimen by including all the defects (Figure 3.3-2), at the corresponding locations. The accuracy of the FE results is restricted by the refinement of the mesh, chosen to be not far from that of the uCT accuracy (the size of the elements was 30÷40 μm). The effect of the high degree of irregularity of the as-built geometry on the stress distribution is qualitatively shown in Figure 3.4-1, by comparing the von Mises equivalent stress distribution in the as-designed unit cell with that of two as-built junctions. The symmetry of the stress distribution is completely lost, and the maximum intensity is reached only in a specific location. Nevertheless, it is clearly shown that the most stressed part of the as-built lattice is close to the junction in all cases (red zones). The values of the

stress concentration factors calculated form the simulations are reported in Table 3.4-4, expressed as the mean value and standard deviation of the values measured for a range of the smallest element sizes. Somewhat surprisingly, they show an increase of only roughly 21% on average, compared to the as-designed geometry, although a wide variability is found. Notably, the junctions situated further away from the specimen axis (J6, J7 and J8), show higher stress concentrations. This is most likely due to the boundary conditions, as will be discussed further later. These results indicate that the as-built junctions are in fact more severe than the as-designed junctions, but not as much as expected from the fatigue tests. Clearly, there are several factors that influence the fatigue strength of the lattice, other than the junctions included in the simulations:

1) only a limited number of junctions was analyzed (there may be more severe junctions that are responsible for the failure of the specimens);
2) detrimental tensile residual stresses, which were in fact measured acting in the axial direction as described in Section 3.2;
3) the unexpectedly high fatigue notch factor K_f^* displayed by the HIPed lattice, even higher than that of the as-built condition, can be imputed to the presence of brittle alpha case, shown in Figure 3.4-2, that increases the sensitivity of the structure to surface cracks (Dallago 2018). The presence of alpha case on the surface of the lattice may be due to the inevitable O contamination of the Ar protective atmosphere in which the HIP treatment was conducted. This suggests the idea that the fatigue strength is more dictated by intrinsic geometric defects rather than the internal porosity, for whose elimination the HIP treatment was devised.
4) possible presence of a brittle alpha case in the HIPed lattice, as shown in Figure 3.4-2, that increases the sensitivity of the structure to surface cracks (Dallago 2018);
5) small distortion of the specimen that may introduce a bending load once the specimen is mounted in the fatigue testing machine that is added to the axial stresses;
6) The smoothing procedure that was necessary to make it possible to mesh the uCT data has in fact decreased the severity of the notches to a certain degree. It is very difficult to quantify this effect because, on the other hand, the discretization of the geometry with voxels produces an unrealistically rough surface.

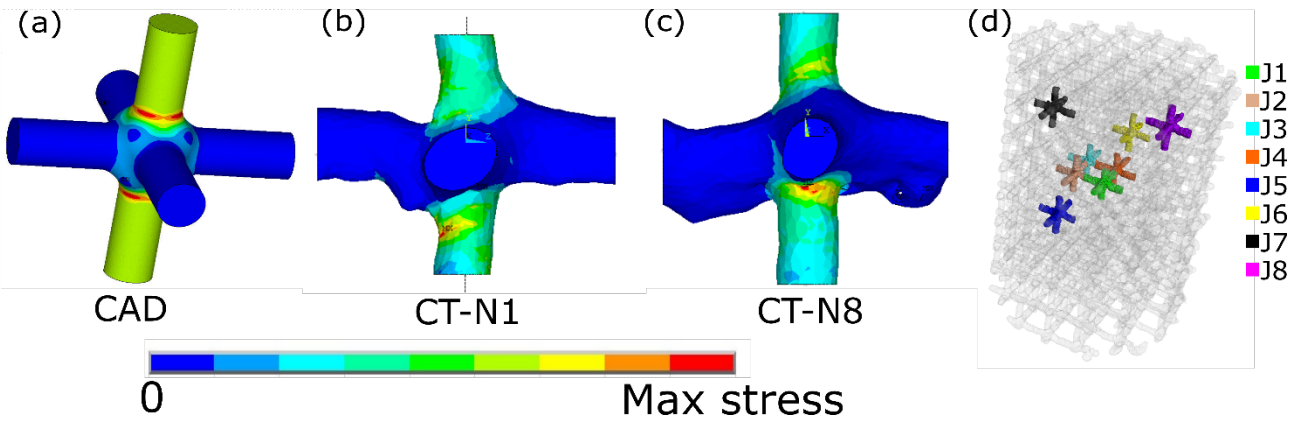

Figure 3.4-1. Von Mises contour plots obtained from the FE analyses. (a) As-designed geometry; (b) junction N. 1; (c) junction N. 8; (d) location of the junctions in the specimen.

Table 3.4-4. K^*_t calculated from the solid FE models based on the CT unit cells: mean value (μ), standard deviation (σ) and % deviation on the K^*_t between the CT and the CAD (K^*_t = 65) based FE models.

Junction	Average (K^*_t uCT)	Std. dev. (K^*_t uCT)	ΔK^*_t uCT vs CAD
J1	76.02	1.1	21.9%
J2	53.14	1.4	-14.7%
J3	76.75	4.5	23.1%
J4	68.54	0.9	9.9%
J5	76.80	1.0	23.2%
J6	85.00	1.3	36.3%
J7	88.90	1.0	42.7%
J8	80.34	3.8	28.9%
Average	75.67	10.9	21.4%

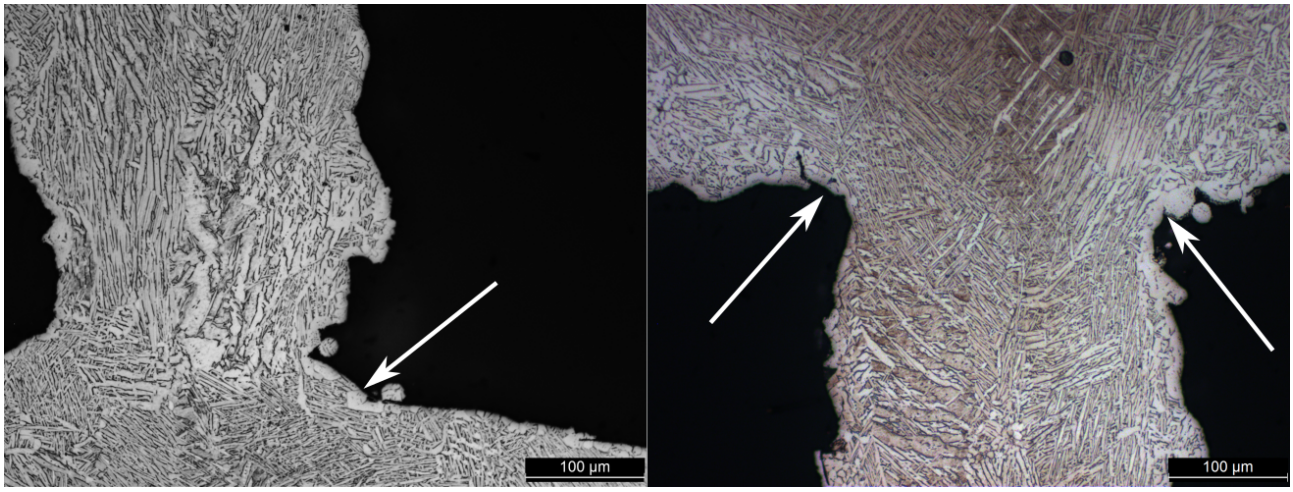

Figure 3.4-2. Microstructure of the HIPed specimens: α phase in a β matrix. The arrows indicate the α phase on the surface (α-case).

An interesting aspect to consider is the effect of the distortion and of the finite size of the specimen on the stress concentration at the junctions. We tried give an estimate by comparing the stress distribution in the as-built junction when the periodic boundary conditions (PBC) are applied with that obtained with the boundary conditions applied as displacements corresponding to the position of each CT unit cell extracted from the beam model of the specimen that includes all the defects. The results of the convergence analysis for each of the eight junctions for both types of boundary conditions are shown in Figure 3.4-3, in terms of the stress concentration factor plotted against the element size. As observed previously, there is a strong variability of the results, but the stress concentration is always lower for the PBC. In Table 3.4-5, the differences between the stress concentration factor calculated with the PBC and the specimen BC are listed both in terms of absolute value and in percentage. The non-symmetrical loading found in the as-built structure further increases the severity of the junctions. Junctions further away from the mid-axis of the specimen (J6, J7 and J8) are more affected by the boundary conditions, as already observed. Figure 3.4-3 allows us to make some observations on the difficulties and on the limitations of this analysis.

To achieve a sufficiently regular mesh, the point cloud representing each junction had to be smoothed at the expense of the finer surface details. In some cases (J1 for example), the convergence plateau for the smallest element size is not observed. This might be related to a difficulty in controlling the element size during meshing operations.

Table 3.4-5. Effect of the finite size of the specimen: variation of the stress concentration factors in the as-built junctions when switching from the BCs extracted from the beam model to the PBCs.

Junction	ΔK^*_t	ΔK^*_t (%)
J1	-6.11	-8.74%
J2	-	-
J3	-1.96	-2.62%
J4	-3.99	-6.19%
J5	-4.32	-5.96%
J6	-10.70	-14.40%
J7	-12.25	-15.98%
J8	- 26.10	-48.11%

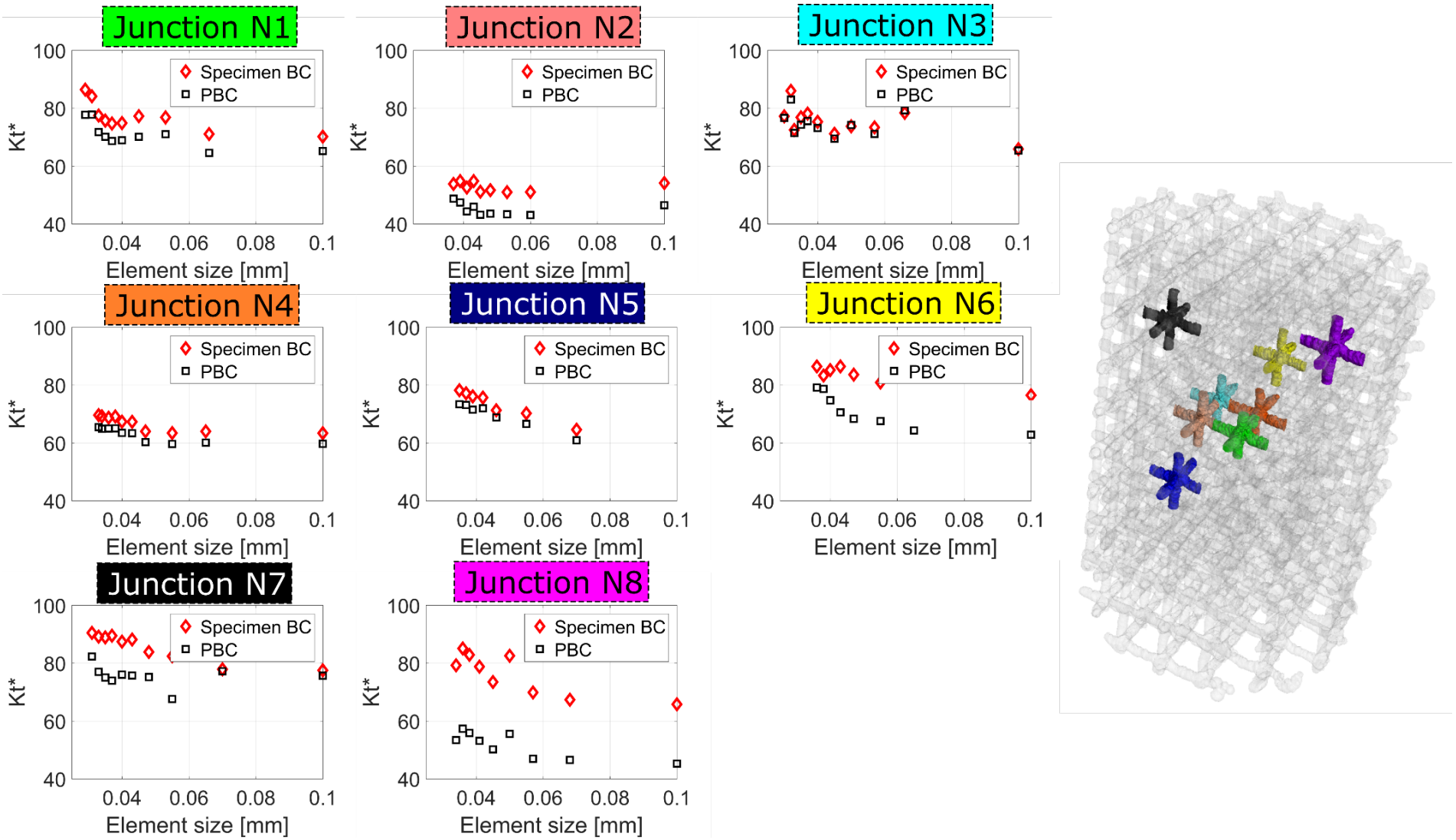

Figure 3.4-3. Convergence analysis of each as-built junction for the two types of BCs (displacements exported from the most realistic beam model and PBCs).

4. Conclusions

In this work, we investigated the effect of geometrical defects and residual stresses on the elastic modulus and on the fully reversed fatigue resistance at 10^6 of regular cubic SLM Ti6Al4V cellular specimens. The geometrical defects of the as-built lattice and the general as-built/as-designed morphological mismatch was discussed on the basis a statistical analysis of the results of the uCT scan of a specimen. FE simulations were completed by importing the as-designed geometry and the as-built geometry acquired with the uCT into ANSYS ®. The results of the experimental measurements were then compared with the FE results and the effect of the as-built/as-designed morphological mismatch on the mechanical behavior was discussed.

The results obtained in this work allow us to draw the following conclusions:

- There is remarkable morphological mismatch between the as-built and the as-designed lattice structure. During printing, the distribution of the material does not depend only on the as-designed geometry fed to the machine but also on the parameters of the process and on the local variations of the thermal properties of the system. In other words, we observe that struts with a different orientation to the printing direction are reproduced with a different accuracy. More specifically, struts with a low angle to the printing plane are systematically affected by an overhang of accumulated molten material that increases the as-built thickness and offsets the barycenter of the cross-sections from the imaginary axis that connects the two junctions introducing a sort of "waviness". The uneven distribution of material affects also the strut junctions by slightly displacing their barycenter and by introducing sharp notches.
- The as-built/as-designed morphological mismatch has a complex influence on the elastic modulus of the lattice. We could say that, in general, the higher thickness of the as-built struts increases the elastic modulus while the bending actions introduced by the strut waviness and the junction center displacement reduce the elastic modulus. Note that a stretching dominated structure such as the one of this study is particularly sensitive to these effects, likely more than a bending dominated structure.
- The fully reversed fatigue resistance appears to be more sensitive to the surface irregularities such as the sharp notches at the strut junctions than internal porosity. As a matter of fact, we observed that HIPing does not have a clear effect on fatigue resistance because, even if it considerably reduces the porosity of the struts [Dallago, 2018], it does not change the surface notches.
- FE analyses of the stress distribution at the strut junctions indicate that the as-built junctions induce a higher stress concentration, although not as high as expected from the experimental analyses. Most likely, fatigue strength is negatively influenced by other factors such as tensile residual stresses, which have been measured even after stress relieving.

The comparison between the mechanical properties predicted considering the as-designed geometry and those measured experimentally highlights the fact that the mechanical behavior of SLM cellular is strongly influenced by the defects (notches, as-built/as-designed geometrical mismatch) introduced by the manufacturing process. In other words, an in-depth knowledge of the characteristics of the manufacturing process is essential to design cellular structures.

5. References

Ahn, Y.-K., Kim, H.-G., Park, H.-K., Kim, G.-H., Jung, K.-H., Lee, C.-W., Kim, W.-Y., Lim, S.-H., Lee, B.-S., 2017. Mechanical and microstructural characteristics of commercial purity titanium implants fabricated by electron-beam additive manufacturing. Mater. Lett. 187, 64–67.

Ashby, M. F., 2006. The properties of foams and lattices, Phil. Trans. R. Soc. A 364, pp. 15-30.

Bagheri, Z. S., Melancon, D., Liu, L., Johnston, R. B., Pasini, D., 2017. Compensation strategy to reduce geometry and mechanics mismatches in porous biomaterials built with Selective Laser Melting. Journal of the Mechanical Behavior of Biomedical Materials 70, pp. 17–27.

Banhart, J., Brinkers, W., 1999. Fatigue behavior of aluminum foams, Journal of Materials Science Letters 18, No. 8, pp. 617-619

Benedetti, M., Torresani, E., Leoni, M., Fontanari, V., Bandini, M., Pederzolli, C., Potrich, C., 2017. The effect of post-sintering treatments on the fatigue and biological behavior of Ti-6Al-4V ELI parts made by selective laser melting, J. Mech. Behav. Biomed. Mater. 71, pp. 295–306.

van den Bogert, A. J., Read, L., Nigg, B. M., 1999. An analysis of hip joint loading during walking, running, and skiing, Med Sci Sports Exerc 31, No. 1, pp. 131-142

Dabrowski, B., Swieszkowski, W., Godlinski, D., Kurzydlowski, K.J., 2010. Highly porous titanium scaffolds for orthopaedic applications. J. Biomed. Mater. Res. B: Appl. Biomater. 95B (1).

Dallago, M., Fontanari, V., Torresani, E., Leoni, M., Pederzolli, C., Potrich, C., Benedetti, M., 2018. Fatigue and biological properties of Ti-6Al-4V ELI cellular structures with variously arranged cubic cells made by selective laser melting, Journal of the Mechanical Behavior of Biomedical Materials 78, pp. 381–394.

Dowling, N. E., 2013. Mechanical Behavior of Materials, Fourth Ed., Pearson

Emmelmann, C., Scheinemann, P., Munsch, M., Seyda, V., 2011. Laser Additive Manufacturing of Modified Implant Surfaces with Osseointegrative Characteristics, Physics Procedia 12, pp. 375–384.

Fleck, N. A., Deshpande, V. S., Ashby, M. F., 2010. Micro-architectured materials: past, present and future, Proc. R. Soc. A 466, pp. 2495-2516

Fricke, W, 2003. Fatigue analysis of welded joints: state of development, Marine Structures 16, pp. 185-200

Gibson, L. J., Ashby, M. F., 1997. Cellular solids - Structures and properties, 2nd edn. Cambridge, Cambridge University Press

Gibson, L. J., 2000. Mechanical behavior of metallic foams, Annu. Rev. Mater. Sci. 30, pp. 191-227

Hedayati, R., Hosseini-Toudeshky, H., Sadighi, M., Mohammadi-Aghdam, M., Zadpoor, A. A., 2016. Computational prediction of the fatigue behavior of additively manufactured porous metallic biomaterials, International Journal of Fatigue 84, pp. 67-79

Hrabe, N.W., Heinl, P., Flinn, B., Körner, C., Bordia, R.K., 2011. Compression-compression fatigue of selective electron beam melted cellular titanium (Ti-6Al-4V). J. Biomed. Mater. Res. Part B 99B, 313–320.

Kessler, J., Balc, N., Gebhardt, A., Abbas, K., 2017. Basic design rules of unit cells for additive manufactured lattice structures. MATEC Web of Conferences 137, 02005

Khademzadeh, S., Carmignato, S., Parvin, N., Zanini, F., Bariani P. F., 2016. Micro porosity analysis in additive manufactured NiTi parts using micro computed tomography and electron microscopy. Materials & Design, vol. 90, pp. 745-752

Khanoki, S.A., Pasini, D., 2012. Multiscale Design and Multiobjective Optimization of Orthopedic Hip Implants with Functionally Graded Cellular Material. Journal of Biomechanical Engineering 134

Khanoki, S.A., Pasini, D., 2013. Fatigue design of a mechanically biocompatible lattice for a proof-of-concept femoral stem. J. Mech. Behav. Biomed. Mater. 22, 65–83.

Kim H. S., Al-Hassani S. T. S., 2003. Effective elastic constants of two-dimensional cellular materials with deep and thick cell walls. International Journal of Mechanical Sciences 45, pp. 1999-2016

de Krijger, J., Rans, C., Van Hooreweder, B., Lietaert, K., Pouran, B., Zadpoor, A.A., 2017. Effects of applied stress ratio on the fatigue behavior of additively manufactured porous biomaterials under compressive loading. J. Mech. Behav. Biomed. Mater. 70, pp. 7–16.

Leuders, S., Thoene, M., Riemer, A., Niendorf, T., Troester, T., Richard, H. A., Maier, H. J., 2013. On the mechanical behaviour of titanium alloy Ti6Al4V manufactured by selective laser melting: Fatigue resistance and crack growth performance, International Journal of Fatigue 48, pp. 300-307

Liu, L., Kamm, P., Garcia-Moreno, F., Banhart, J., Pasini, D., 2017. Elastic and failure response of imperfect three-dimensional metallic lattices: the role of geometric defects induced by Selective Laser Melting, Journal of the Mechanics and Physics of Solids 107, pp. 160–184.

Long, M., Rack, H.J., 1998. Titanium alloys in total joint replacement - a materials science perspective. Biomaterials 19, 1621–1639.

Maxwell, D. C., Nicholas, T., 1999. A rapid method for generation of a Haigh diagram for high cycle fatigue, Fatigue and Fracture Mechanics: Twenty-Ninth Volume, ASTM STP 1332, Panontin T. L. and Sheppard S. D., Eds., American Society for Testing Materials, West Conshohocken, PA

Mullen, L., Stamp, R. C., Brooks, W. K., Jones, E., Sutcliffe, C. J., 2009. Selective Laser Melting: A Regular Unit Cell Approach for the Manufacture of Porous, Titanium, Bone In-Growth Constructs, Suitable for Orthopedic Applications, J Biomed Mater Res B Appl Biomater 89(2), pp. 325–334.

Murr, L. E., Gaytan, S. M., Medina, F., Martinez, E., Martinez, J. L., Hernandez, D. H., Machado, B. I., Ramirez, D. A., Wicker, R. B., 2010. Characterization of Ti6Al4V open cellular foams fabricated by additive manufacturing using electron beam melting, Materials Science and Engineering A 527, pp. 1861-1868

Murr, L. E., Gaytan, S. M., Ramirez, D. A., Martinez, E., Hernandez, J., Amato, K. N., Shindo, P. W., Medina, F. R., Wicker, R. B., 2012. Metal fabrication by additive manufacturing using laser and electron beam melting technologies, J. Mater. Sci. Technol. 28, No. 1, pp. 1-14

Niinomi, M., 2008. Mechanical biocompatibilities of titanium alloys for biomedical applications. J. Mech. Behav. Biomed. Mater. 1, 30–42.

Parthasarathy, J., Starly, B., Ramana, S., Christensen, A., 2010. Mechanical evaluation of porous titanium (Ti6Al4V) structures with electron beam melting (EBM), Journal of the Mechanical Behavior of Biomedical Materials 3, pp. 249–259.

Pyka, G., Kerckhofs, G., Papantoniou, I., Speirs, M., Schrooten, J., Wevers, M., 2013. Surface Roughness and Morphology Customization of Additive Manufactured Open Porous Ti6Al4V Structures, Materials 6, pp. 4737–4757.

Qiu, C., Adkins, N. J. E., Attallah, M. M., 2013. Microstructure and tensile properties of selectively laser-melted and HIPed laser-melted Ti6Al4V, Materials Science & Engineering A 578, pp. 230-239

Qiu, C., Yue, S., Adkins, N. J. E., Ward, M., Hassanin, H., Lee, P. D., Withers, P. J., Attallah, M. M., 2015. Influence of processing conditionson strut structure and compressive properties of cellular lattice structures fabricated by selective laser melting, Materials Science & Engineering A 628, pp.188–197.

Rack, H.J., Qazi, J.I., 2006. Titanium alloys for biomedical applications. Mater. Sci. Eng. C 26, 1269–1277.

Rashed, M. G., Ashraf, M., Mines, R. A. W., Hazell, P. J., 2016. Metallic microlattice materials: A current state of the art on manufacturing, mechanical properties and applications, Materials and Design 95, pp. 518-533

Ryan, G., Pandit, A., Apatsidis, D. P., 2006. Fabrication methods of porous metals for use in Orthopaedic applications, Biomaterials 27, pp. 2651-2670

Schajer, G., Winiarski, B, Withers, PJ, Hole-drilling Residual Stress Measurement with Artifact Correction Using Full-field DIC Experimental Mechanics, 2013. 53(2): p. 255-265.

Sing, S. L., Wiria, F. E., Yeong, W. Y., 2018. Selective laser melting of lattice structures: A statistical approach to manufacturability and mechanical behavior, Robotics and Computer–Integrated Manufacturing 49, pp. 170–180.

Singh, R., Lee, P. D., Dashwood, R. J., Lindley, T. C., 2010. Titanium fomas for biomedical applications: a review, Materials Technology 25, No. ¾

Tammas-Williams, S., Withers, P.J., Todd, I., Prangnell, P.B., 2016. The effectiveness of hot isostatic pressing for closing porosity in titanium parts manufactured by selective electron beam melting. Metall. Mater. Trans. A 47A.

Tan, X.P., Tan, Y.J., Chow, C.S.L., Tor, S.B., Yeong, W.Y., 2017. Metallic powder-bed based 3D printing of cellular scaffolds for orthopaedic implants: a state-of-the-art review on manufacturing, topological design, mechanical properties and biocompatibility. Mater. Sci. Eng. C 76, 1328–1343.

Van Bael, S., Kerckhofs, G., Moesen, M., Pyka, G., Schrooten, J., Kruth, J.P., 2011. Micro-CT-based improvement of geometrical and mechanical controllability of selective laser melted Ti6Al4V porous structures, Materials Science and Engineering A 528, pp. 7423–7431.

Van Hooreweder, B., Apers, Y., Lietaert, K., Kruth, J.-P., 2017. Improving the fatigue performance of porous metallic biomaterials produced by Selective Laser Melting, Acta Biomaterialia 47, pp. 193-202

Vrancken, B., Thijs, L., Kruth, J.-P., Van Humbeeck, J., 2012. Heat treatment of Ti6Al4V produced by Selective Laser Melting: microstructure and mechanical properties. J. Alloy. Compd. 541, 177–185

Wauthle, R., Vrancken, B., Beynaerts, B., Jorissen, K., Schrooten, J., Kruth, J.-P., Van Humbeek, J., 2015. Effects of build orientation and heat treatment on the microstructure and mechanical properties of selective laser melted Ti6Al4V lattice structures, Additive manufacturing 5, pp. 77-84

Winiarski, B., Schajer, GS, Withers, PJ, Surface Decoration for Improving the Accuracy of Displacement Measurements by Digital Image Correlation in SEM. Experimental Mechanics, 2012. 52(7): p. 793-804.

Winiarski, B., Withers, PJ, Micron-Scale Residual Stress Measurement by Micro-Hole Drilling and Digital Image Correlation. Experimental Mechanics, 2012. 52(4): p. 417-428.

Wits, W. W. et al, 2016. Porosity testing methods for the quality assessment of selective laser melted parts, CIRP Annals Man. Tech. 65(1), pp. 201-204

Wu, S., Liu, X., Yeung, K. W. K., Liu, C., Yang, X., 2014. Biomimetic porous scaffolds for bone tissue engineering, Materials Science and Engineering R 80, pp. 1-36

Yan, C., Hao, L., Hussein, A., Young, P., Raymont, D., 2014. Advanced lightweight 316L stainless steel cellular lattice structures fabricated via selective laser melting Materials and Design 55, pp. 533–541.

Yavari, S. A., Ahmadi, S. M., Wauthle, R., Pouran, B., Schrooten, J., Weinans, H., Zadpoor, A. A., 2015. Relationships between unit cell type and porosity and the fatigue behavior of selective laser melted meta-biomaterials, Journal of the mechanical behavior of biomedical materials 43, pp. 91-100

Zargarian, A., Esfahanian, M., Kadkhodapour, J., Ziaei-Rad, S., 2016. Numerical simulation of the fatigue behavior of additive manufactured titanium porous lattice structures, Materials Science and Engineering C 60, pp. 339-347

Zenkert, D., Shipsha, A., Burman, M., 2006. Fatigue of closed cell foams, Journal of Sandwich Structures and Materials 8, pp. 517-538

Zettl, B., Mayer, H., Stanzl-Tschegg, S. E., Degischer, H. P., 2000. Fatigue properties of aluminum foams at high numbers of cycles, Materials Science and Engineering A292, pp. 1-7

Zhao, S., Li, S. J., Hou, W. T., Hao, Y. L., Yang, R., Misra, R. D. K., 2016a. The influence of cell morphology on the compressive fatigue behavior of Ti6Al4V meshes fabricated by electron beam melting, Journal of the Mechanical Behavior of Biomedical Materials 59, pp. 251-264

Zhao, S., Li, S. J., Hou, W. T., Hao, Y. L., Yang, R., Murr, L. E., 2016b. Microstructure and mechanical properties of open cellular Ti6Al4V prototypes fabricated by electron beam melting for biomedical applications, Materials Technology: Advanced Performance Materials 31, No. 2

Zhu, Z., Anwer, N., Mathieu, L., 2017. Deviation Modeling and Shape transformation in Design for Additive Manufacturing, Procedia CIRP 60, pp. 211–216.